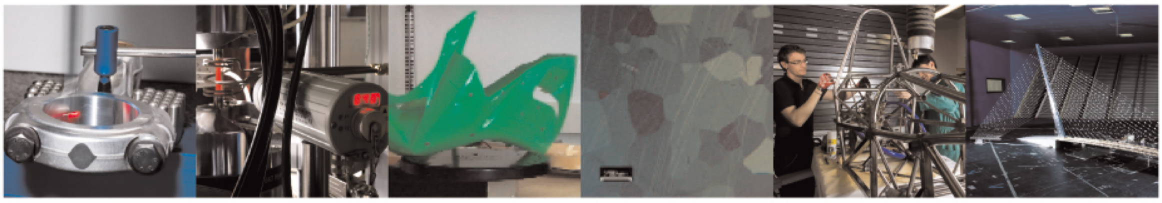

Real-Time In-Service Load Tracking Toward Airframe Digital Twins

Zhou,Xuan;Dong, Leiting;Dziendzikowski, Michal;Dragan, Krzysztof;Giglio, Marco;Sbarufatti, Claudio

This is a post-peer-review, pre-copyedit version of Real-Time In-Service Load Tracking Toward Airframe Digital Twins, Xuan Zhou, Leiting Dong, Michal Dziendzikowski, Krzysztof Dragan, Marco Giglio, and Claudio Sbarufatti, AIAA Journal 2025 63:12, 5416-5429.

Real-Time In-Service Load Tracking Toward Airframe Digital Twins

Xuan Zhou * and Leiting Dong†
Beihang University, 100191 Beijing, People's Republic of China

Michal Dziendzikowski‡ and Krzysztof Dragan§
Air Force Institute of Technology, 01-494 Warszawa, Poland

Marco Giglio¶ and Claudio Sbarufatti‖
Polytechnic University of Milan, 20156 Milan, Italy

Accurate load monitoring is essential for constructing reliable load spectra of aeronautical structures, driving the evolution of airframe digital twins during service. However, onboard strain sensors are often omitted in many aircraft due to weight, reliability, and cost constraints, making accurate load tracking challenging. This study proposes an innovative approach combining deep-learning-based strain prediction with an improved inverse-direct method for the in-service load tracking of sensor-limited aircraft. First, a deep-learning model incorporating time-series features is trained on flight test data. It uses flight parameters as input to predict strain at discrete, limited locations with high accuracy, outperforming conventional regression methods. Second, an improved inverse-direct load monitoring approach using reduced-order aerodynamic modes as physically interpretable basis functions is introduced, which enhances the load monitoring accuracy with discrete strain measurement. During service, the strain prediction model integrates with the inverse-direct method, enabling real-time full-field load and deformation tracking using only flight parameters, thus bypassing the need for an extensive sensor network. Experimental validation on a 3.2-m-wingspan unmanned aerial vehicle demonstrates superior performance, highlighting the effectiveness of this strain sensor-free methodology. This approach offers a practical pathway for retrofitting existing fleets with airframe digital twin capabilities, while preserving original airframe configurations.

Nomenclature

---

*Assistant Professor, School of Aeronautic Science and Engineering; Also affiliated with Tianmushan Laboratory, 310023 Hangzhou, People's Republic of China; he was a PhD student at the Department of Mechanical Engineering, Polytechnic University of Milan, 20156 Milan, Italy.

†Professor and Chairman of School Council, School of Aeronautic Science and Engineering; Also affiliated with the Tianmushan Laboratory, 310023 Hangzhou, People's Republic of China; Co-corresponding author: ltdong@buaa.edu.cn

‡Researcher, Airworthiness Division.

§Chief of Department, Airworthiness Division

¶Professor, Department of Mechancial Engineering.

‖Associate Professor, Department of Mechancial Engineering; Corresponding author: claudio.sbarufatti@polimi.it

ε = strain

$\boldsymbol{\alpha}$ = calibration matrix

$\boldsymbol{\alpha}_0$ = bias vector

$\mathbf{F}$ = deformation

$\mathbf{L}$ = aerodynamic load

$\mathbf{N}$ = linear transformation matrix

$\mathbf{V}$ = indicated airspeed

α = angle of attack

β = side-slip angle

p, q, r = rate of roll, pitch and yaw

$\mathbf{p}$ = flight parameters

δ = aileron deflection

$\Delta\mathbf{T}$ = temperature change

Superscripts

meas = measurement

sim = simulation

$+$ = pseudo-inverse

Subscripts

FBG = fibre bragg grating sensor

ft = flight test

rd = reduced-dimensional

tot = total, consisting the variables of load and temperature

l = left

r = right

I. Introduction

Aircraft experience continuous aerodynamic loads throughout flight, resulting in structural deformation and potential fatigue damage initiation and growth [1]. In 2012, the National Aeronautics and Space Administration (NASA) and the Air Force Research Laboratory (AFRL) introduced the concept of airframe digital twins [2, 3], which has since gained widespread attention in the aerospace field [4–7]. A Digital Twin is an integrated multiphysics, multiscale, probabilistic simulation of an as-built vehicle or system that uses the best available physical models, sensor updates, fleet history, etc., to mirror the life of its corresponding flying twin [3]. For airframe digital twins, tracking the load history during flight [8], along with comprehensive assessments of structural deformation, is essential for monitoring structural fatigue [9, 10] and evaluating risks at critical locations [11–14]. Several methodologies for load tracking have emerged, including strain-based monitoring [15], data-driven load prediction [16], and simulation-based prediction [17].

Strain-based load monitoring methods involve strategically deploying sensors on the structure to directly measure strains and acquire load information at critical locations [18, 19]. These techniques primarily rely on structural models, employing approaches such as the inverse Finite Element Method (iFEM) [20] and inverse-direct methods [15, 21]. While discrete strain measurements demonstrate high accuracy in isolated scenarios, the primary challenge lies in capturing the full-field load distribution across an aircraft, often requiring a significant number of sensors and careful selection of the basis function for load distribution [22].

Data-driven load prediction relies on aircraft flight parameters, capturing pilot control actions and flight state changes during flight. With the majority of in-service aircraft equipped with flight data recorders, which document the time history of flight parameters, a correlation between flight parameters and structural loads can be established [16]. In the current paradigm of individual load tracking [23], strain sensors are typically attached to a limited number of test aircraft during the flight test stage. The simultaneous collection of flight parameters and strain data is used to construct a surrogate model, often employing multiple linear regression or artificial neural networks [24]. Subsequently, during the service stage, real-time flight data from various aircraft is utilized to predict loads at critical locations.

Deep learning methods, such as Convolutional Neural Networks (CNN) [25] and Long Short-Term Memory (LSTM) networks [26], have shown promise in addressing time-series prediction tasks, which can be adopted to improve the prediction accuracy. Load prediction methods rooted in deep learning have been explored in various fields. In civil engineering, for instance, Zhang et al. [27] applied the LSTM to predict the nonlinear seismic response of building structures, using earthquake wave signals as inputs and predicting structural responses as outputs. Similarly, Gulgec et al. [28] employed the LSTM method, utilizing collected acceleration responses as inputs to estimate strain responses on a horizontal cantilever beam in a controlled laboratory setting. However, applying load prediction to aircraft structures presents heightened challenges due to the complexity of aircraft structures and the variability of the flight environment. Aircraft structures exhibit greater intricacies, and the dynamic nature of the flight environment significantly increases the difficulty of load prediction.

Simulation-based prediction involves utilizing data from a flight parameter recorder and employing surrogate models derived from simulation techniques such as flight mechanics, computational fluid dynamics, and finite element analysis. This approach aims to forecast loads and stresses at critical locations on the aircraft [17, 29]. In contrast to strain-based methods, these simulation-dependent approaches replicate real loading sequences, providing detailed load distribution information that enhances the insight of airframe digital twins. However, the accuracy of this method hinges on the fidelity of the model, posing challenges in ensuring the credibility of predictions [17]. However, while aerodynamic simulations may exhibit inaccuracies in absolute load magnitudes, they can still yield valuable distribution patterns that inform the load tracking.

To tackle the challenge outlined above and consider the complexities involved in installing strain sensors during the service stage compared to the flight test stage, this study introduces an innovative strain-sensor-free in-service load tracking approach. This approach integrates deep-learning-based prediction with inverse-direct monitoring and is validated using realistic flight test data obtained from a 3.2 m wingspan unmanned aerial vehicle (UAV). The findings illustrate the method's capacity to yield outcomes comparable to load tracking based on strain measurements, thereby offering significant implications for its application in the aircraft service stage. The primary contributions of this paper are summarized as follows:

1) Introduce an improved inverse-direct load monitoring method that utilizes reduced-dimensional aerodynamic load representation as the physically interpretable basis function and incorporates a temperature compensation strategy, providing a more physical and accurate inversion of load distribution.
2) Explore deep learning methods for constructing a discrete strain prediction model, with an emphasis on the time-series characteristics of the flight and strain data. It uses flight parameters as input to predict strain at discrete, limited locations with high accuracy, outperforming conventional regression methods.
3) Propose an innovative in-service flight load tracking approach that combines deep-learning prediction with inverse-direct monitoring, which provides an efficient and accurate means of predicting full-field loads during the service stage, bypassing the need for an extensive strain sensor network.

The remainder of this paper is organized as follows: Section II integrates an enhanced inverse-direct load monitoring approach with data-driven load prediction methods, presenting an in-service load tracking framework. Section III applies the proposed framework to a UAV. The load tracking results are presented in Section IV, followed by discussions on the affecting factors in Section V. The paper concludes in Section VI with final remarks.

II. In-Service Load Tracking Combining Deep-learning-based Prediction and Inverse-direct Monitoring

In this section, an innovative in-service flight load tracking framework is proposed, which offers a significant advantage by enabling full-field prediction of flight loads and structural deformation of the aircraft during the service stage using only flight parameters, thus eliminating the need for additional sensors. This integration is achieved by utilizing flight parameter and strain measurement collected during the flight test stage, and the aerodynamic and structural model simulation models at the design stage. The fundamental flow of the proposed framework is illustrated in Fig. 1, and it comprises two distinct stages.

In the offline stage, first, batch aerodynamic and structural simulations are conducted to generate multiple samples of aerodynamic load distributions and the corresponding simulated strains at the measurement locations. Principal

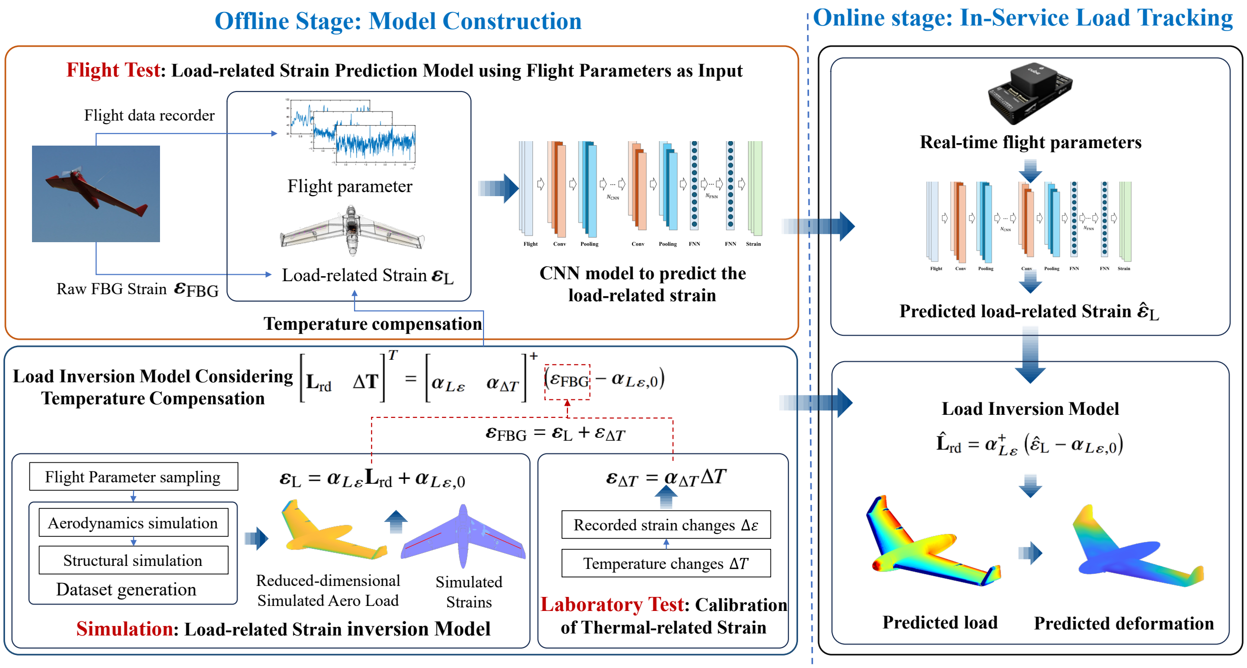

Fig. 1 **In-service flight load tracking combines the flight test data and inverse-direct load monitoring.**

Component Analysis (PCA) is then applied to reduce the dimensionality of the aerodynamic load, extracting a set of basis coefficients. This enables the establishment of a relationship between the reduced-dimensional aerodynamic load and the measured strain.

Secondly, during the laboratory test, temperature variations are recorded along with the corresponding strain changes at the Fiber Bragg Grating (FBG) sensor locations. This allows the derivation of a relationship between temperature fluctuations and thermally induced strain. By integrating these two components of the FBG strain, a load inversion model incorporating temperature compensation is developed.

Thirdly, in the flight test stage, flight parameters are recorded using the flight data recorder. The raw strain measurements are processed through the load inversion model, incorporating temperature compensation, to extract the load-related strain. A Convolutional Neural Network (CNN) model is then trained with flight parameters as input and load-related strain as output.

Finally, in the online stage, real-time flight parameters serve as inputs to the CNN model, which predicts the discrete, load-related strain., which is subsequently fed into the load inversion model to estimate the aerodynamic load distribution. Additionally, the deformation distribution is predicted using the mapping between aerodynamic load and deformation, which, for small, low-speed aircraft, can be approximated as a linear relationship.

A. Simulation-based Load inversion with a Reduced-dimensional Aerodynamics Representation

In this subsection, a simulation-based load inversion model, which is a modification of the previous study in [15, 21], is used to invert the aerodynamic load on the aircraft with the strain measurement in discrete, limited locations. The novelty behind the proposed method comes from the reduced-order aerodynamic load representation, which replaces the original equivalent load set, presents a more physical representation of the load distribution in the load inversion. The construction process of the flight tracking model is graphically depicted in Fig. 2.

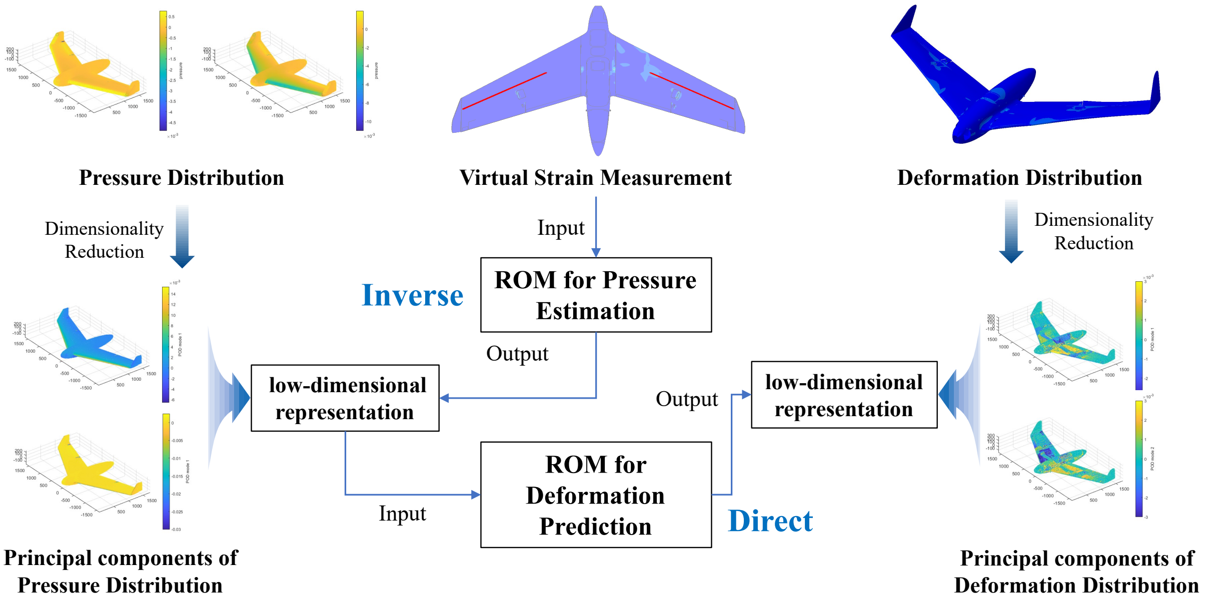

Fig. 2 Workflow for generating the improved inverse-direct load monitoring model using the simulation database.

Prior to the inverse-direct process, the aerodynamic and structural models are utilized to construct a simulation database. This database contains the aerodynamic load distribution $\mathbf{L}^{\mathrm{sim}}$, the deformation field distribution $\mathbf{F}^{\mathrm{sim}}$, and the virtual sensing value $\boldsymbol{\varepsilon}_L^{\mathrm{sim}}$ corresponding to each strain sensor sample can be extracted.

Subsequently, the inverse-direct method, which employs reduced-order aerodynamic loads with linear regression, is divided into two distinct stages: the inverse load inversion process and the direct deformation prediction process. The inverse load estimation is addressed first.

The relationship between load-related strain $\boldsymbol{\varepsilon}_{\mathrm{L}}$ and aerodynamic loads $\mathbf{L}$ can be expressed as a linear relationship for most aircraft structures without a high aspect ratio:

$$\boldsymbol{\varepsilon}_L = \mathbf{N}_{L\varepsilon}^{\mathrm{T}}\mathbf{L} \tag{1}$$

where $\mathbf{N}_{L\varepsilon}$ is the linear transformation matrix from aerodynamic loads to strain sensor measurements.

Given that aerodynamic loads are distributed on the outer surface of the aircraft, using discretized meshes with high degrees of freedom makes the dimension of $N_{L\varepsilon}$ too high to build. To address this challenge, the PCA method [30] is utilized to reduce the dimensionality of the aerodynamic load distribution. By projecting the original load distribution $\mathbf{L}$ onto a lower-dimensional subspace, PCA identifies the most significant directions (principal components) that capture the majority of the variation in the load distribution. This reduced-dimensional representation of the aerodynamic loads, $\mathbf{L}_{\mathrm{rd}}$, is obtained by subtracting the mean of the aerodynamic loads $\overline{\mathbf{L}}$ in $\mathbf{L}^{\mathrm{sim}}$ and then applying the projection matrix $\mathbf{U}_{M\times q_L}$, which consists of the first q_L principal components. Here, M represents the degree of freedom (DOF) of the aerodynamic model. Mathematically, the reduced-dimensional aerodynamic loads $\mathbf{L}_{\mathrm{rd}}$ are given by:

$$\mathbf{L}_{\mathrm{rd}} = \mathbf{U}^{\mathrm{T}}_{M\times q_L}(\mathbf{L} - \overline{\mathbf{L}}) \tag{2}$$

Since the principal component analysis is a linear transformation, a linear transformation between strain measurement and principal component coefficients still exists. Substituting Eq. 2 into Eq. 1 yields a mapping model for the low-dimensional representation of the aerodynamic loads $\mathbf{L}_{\mathrm{rd}}$ to the load-related strain $\boldsymbol{\varepsilon}_L$:

$$\boldsymbol{\varepsilon}_L = (\mathbf{U}\mathbf{N}_{L\varepsilon})^{\mathrm{T}}\,\mathbf{L}_{\mathrm{rd}} + \mathbf{N}^{\mathrm{T}}_{L\varepsilon}\overline{\mathbf{L}} = \boldsymbol{\alpha}_{L\varepsilon}\mathbf{L}_{\mathrm{rd}} + \boldsymbol{\alpha}_{L\varepsilon,0} \tag{3}$$

where $\boldsymbol{\alpha}_{L\varepsilon} = \mathbf{N}^{\mathrm{T}}_{L\varepsilon}\mathbf{U}^{\mathrm{T}}$ is known as the calibration matrix. It is a linear operator that maps $\mathbf{L}_{\mathrm{rd}}$ to $\boldsymbol{\varepsilon}_L$. $\boldsymbol{\alpha}_{L\varepsilon,0} = \mathbf{N}^{\mathrm{T}}_{L\varepsilon}\overline{\mathbf{L}}$ is a bias vector caused by the mean value of PCA. Both $\boldsymbol{\alpha}_{L\varepsilon}$ and $\boldsymbol{\alpha}_{L\varepsilon,0}$ can be obtained from the low-dimensional representations of the aerodynamic load distribution in the simulation database $\mathbf{L}^{\mathrm{sim}}_{\mathrm{rd}}$ and the virtual strain sensing $\boldsymbol{\varepsilon}^{\mathrm{sim}}_L$ through linear regression fitting.

When the strain measurement $\boldsymbol{\varepsilon}^{\mathrm{meas}}$ is obtained during the flight test, the predicted $\bar{\mathbf{L}}_{\mathrm{rd}}$ can be obtained by:

$$\hat{\mathbf{L}}_{\mathrm{rd}} = \boldsymbol{\alpha}^{+}_{L\varepsilon}\left(\boldsymbol{\varepsilon}^{\mathrm{meas}} - \boldsymbol{\alpha}_{L\varepsilon,0}\right) \tag{4}$$

where $\boldsymbol{\alpha}^{+}_{L\varepsilon} = \left(\boldsymbol{\alpha}^{\mathrm{T}}_{L\varepsilon}\boldsymbol{\alpha}_{L\varepsilon}\right)^{-1}\boldsymbol{\alpha}^{\mathrm{T}}_{L\varepsilon}$ is the pseudo-inverse matrix of the calibration matrix $\boldsymbol{\alpha}_{L\varepsilon}$.

Once the reduced-dimensional aerodynamic loads are obtained through the inverse estimation process, the full-field deformation of the aircraft can be determined through the direct prediction process. The mapping relationship between the low-dimensional representation of the aerodynamic loads $\mathbf{L}_{\mathrm{rd}}$ and the deformation $\mathbf{F}$ is expressed as follows:

$$\mathbf{F} = \boldsymbol{\alpha}_{LF}\mathbf{L}_{\mathrm{rd}} + \boldsymbol{\alpha}_{LF,0} \tag{5}$$

where $\boldsymbol{\alpha}_{LF} = \mathbf{N}^{\mathrm{T}}_{LF}\mathbf{U}^{\mathrm{T}}$ represents the scaling factor between the reduced-dimensional load and the deformation. $\mathbf{N}_{LF}$ is the matrix of linear transformations from aerodynamic loads to strain measurements and $\boldsymbol{\alpha}_{LF,0}$ is the bias term.

By applying the method outlined in this section, a more physically meaningful inversion of the aerodynamic load distribution can be obtained. A comparative analysis between the proposed approach and the baseline method [15] is presented in Section IV.A. It is important to note that this method is not limited to the linear case discussed in this study. It can also be extended to nonlinear, large-deformation aircraft structures through the integration of nonlinear surrogate models, such as Gaussian Process Regression or Neural Networks.

B. Temperature Compensation Considering Thermal-related Strains in the Laboratory Environment

When performing strain measurements using FBG sensors, it is crucial to account for temperature variations, as these can induce thermal strains that may compromise the accuracy of the measurements [31]. This section outlines a strategy for temperature compensation, as proposed in [15].

Initially, the aircraft is placed in a controlled laboratory environment without external loads for an extended period. The temperature variation, denoted as $\Delta\mathbf{T}$, is monitored using thermometers, while the corresponding thermal-related strain, $\varepsilon_{\Delta T}$, is recorded by the strain sensors. A linear relationship is assumed between the temperature variation and the thermal-related strain:

$$\varepsilon_{\Delta T} = \boldsymbol{\alpha}_{\Delta T}\Delta\mathbf{T} \tag{6}$$

where $\boldsymbol{\alpha}_{\Delta T}$ represents the temperature influence coefficients, which can be determined through a least squares fitting approach:

$$\boldsymbol{\alpha}_{\Delta T} = (\boldsymbol{\varepsilon}_{\Delta T}\boldsymbol{\varepsilon}_{\Delta T}^{T})^{-1}\boldsymbol{\varepsilon}_{\Delta T}^{T}\Delta\mathbf{T}. \tag{7}$$

Then, take the thermal-related strain $\boldsymbol{\varepsilon}_{\Delta T}$ into account in the load inversion model, the FBG strain measurement $\boldsymbol{\varepsilon}_{\text{FBG}}$ during the flight consists of the load-related strain $\boldsymbol{\varepsilon}_{L}$ and thermal-related strain $\boldsymbol{\varepsilon}_{\Delta T}$:

$$\boldsymbol{\varepsilon}_{\text{FBG}} = \boldsymbol{\varepsilon}_{\text{L}} + \varepsilon_{\Delta T} = \begin{bmatrix} \boldsymbol{\alpha}_{L\varepsilon} & \boldsymbol{\alpha}_{\Delta T} \end{bmatrix} \begin{bmatrix} \mathbf{L}_{\text{rd}} \\ \Delta\mathbf{T} \end{bmatrix} + \boldsymbol{\alpha}_{L\varepsilon,0} = \boldsymbol{\alpha}_{\text{tot}}\,\mathbf{L}_{\text{tot}} + \boldsymbol{\alpha}_{L\varepsilon,0} \tag{8}$$

where $\mathbf{L}_{\text{tot}} = \begin{bmatrix} \mathbf{L}_{\text{rd}} \\ \Delta\mathbf{T} \end{bmatrix}$ represents the augmentation vector for the inversion, and $\boldsymbol{\alpha}_{\text{tot}} = \begin{bmatrix} \boldsymbol{\alpha}_{L\varepsilon} & \boldsymbol{\alpha}_{\Delta T} \end{bmatrix}$ is the augmentation matrix corresponding to the calibration matrix.

The load inversion model, as denoted by Eq. (4), has also undergone modifications:

$$\hat{\mathbf{L}}_{\text{tot}} = \boldsymbol{\alpha}_{\text{tot}}^{+}\left(\varepsilon_{\text{FBG}}^{\text{meas}} - \boldsymbol{\alpha}_{L\varepsilon,0}\right) \tag{9}$$

where $\boldsymbol{\alpha}_{\text{tot}}^{+} = \left(\boldsymbol{\alpha}_{\text{tot}}^{\text{T}}\boldsymbol{\alpha}_{\text{tot}}\right)^{-1}\boldsymbol{\alpha}_{\text{tot}}^{\text{T}}$ is the pseudo-inverse matrix of the $\boldsymbol{\alpha}_{\text{tot}}$, $\varepsilon_{\text{FBG}}^{\text{meas}}$ denotes the measured FBG strains during the flight.

Upon obtaining $\hat{\mathbf{L}}_{\text{tot}}$ through the inversion of $\varepsilon_{\text{FBG}}^{\text{meas}}$ measured by strain sensors, simultaneous derivations of the estimated aerodynamic load distribution, $\hat{\mathbf{L}}_{\text{rd}}$, and the estimated temperature change, $\Delta\hat{\mathbf{T}}$, can be achieved. The required deformation can then be predicted according to Eq. 5.

C. Convolutional Neural Network-Based Discrete Strain Prediction Trained on Flight Test Data

In the previous two subsections, we introduced an approach for inverting the aerodynamic load based on discrete strain measurements. However, during the service stage, directly obtaining strain measurement is often challenging. To address this limitation, this subsection presents a data-driven strain prediction model that incorporates time-series dependencies, which would provide the strain information during the service stage.

Specifically, the proposed model utilizes a One-Dimensional Convolutional Neural Network (1D-CNN) as its foundational component. The model is trained using recorded flight parameters $\mathbf{p}_{\text{ft}}^{\text{meas}}$ and load-related strain $\boldsymbol{\varepsilon}_{\text{ft}}^{L}$ obtained from flight tests. The load-related strain is preprocessed using the load inversion model in Section II.B to mitigate thermal effects, thereby ensuring that the predictions more accurately reflect the actual structural loads.

$$\boldsymbol{\varepsilon}_{\text{ft}}^{L} = \boldsymbol{\varepsilon}_{\text{ft}}^{\text{meas}} - \boldsymbol{\varepsilon}_{\text{ft}}^{\Delta T} \tag{10}$$

1D-CNNs are widely used for time-series analysis due to their low computational cost. The simple and compact structure of 1D-CNNs, which primarily employs 1D convolutions (scalar multiplication and addition), allows for real-time and cost-efficient hardware implementations. The strain prediction model developed in this study consists of an input layer, convolutional modules, fully connected layers, and an output layer. Figure 3 illustrates the basic architecture and constituent modules of the model. The input layer includes flight parameters, while the model predicts strain at discrete sensor locations. By varying the number of convolutional modules and fully connected layers, different structural configurations and parameter settings for the strain prediction model can be explored.

During the training process, the network utilizes a dataset comprising paired flight parameter-strain measurement samples. Iterative adjustment of the weights and biases of the network minimizes the disparity between the predicted and actual strain values. The Mean Squared Error (MSE) loss function is employed to guide the network towards optimal parameter learning by measuring the square of the difference between predicted and actual values. The training process utilizes the Adam algorithm, which iteratively updates the network parameters to enhance the efficiency of the learning process.

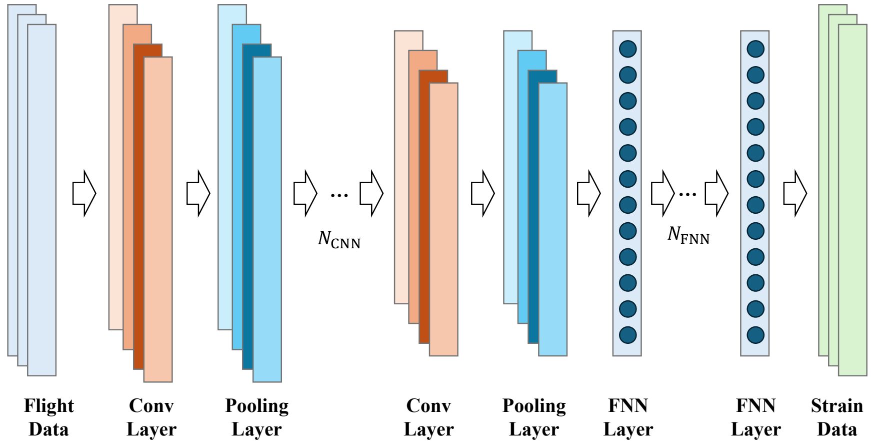

Fig. 3 CNN-based strain prediction neural networks.

D. In-Service Full-Field Load and Deformation Tracking Using Only Flight Parameters

With the implementation of CNN-based discrete strain prediction and improved inverse-direct load monitoring, full-field load and deformation tracking can be achieved during service, as illustrated in Fig. 4. This approach enables real-time prediction of load and deformation distributions (including stress, strain, and displacement) using only flight parameters during the service stage, eliminating the need for a dedicated strain sensor network.

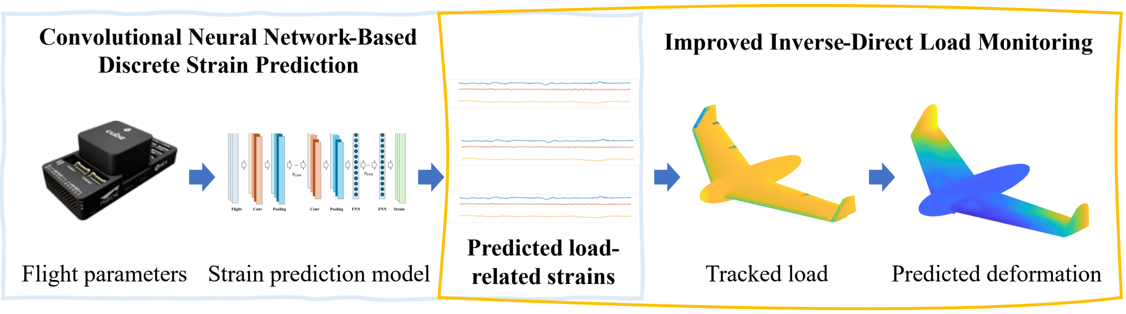

Fig. 4 In-service flight load tracking combines the flight test data and inverse-direct load monitoring.

III. Validation on an Unmanned Aerial Vehicle

In this section, a UAV with a 3.2-meter wingspan is utilized to validate the proposed in-service load tracking approach with real flight data. We begin by outlining the fundamental configuration and flight test details of the UAV, including the gathered flight parameters and strain data collected during the flight test. Subsequently, we delineate the simulation models and the created database of the UAV. The simulation database and the flight dataset are then used to generate the models required for the load tracking.

A. UAV Configuration and Flight Test

The flight test data employed in this study is derived from a full-size UAV. The UAV features a flying wing layout, incorporating a swept-back trapezoidal wing design augmented by wingtiplets. Constructed primarily from composite materials, predominantly fiberglass, the UAV's fuselage measures approximately 1.7 m in length, coupled with a wingspan of about 3.2 m. Additional specifications are detailed in Table 1.

Table 1 Configuration of the Unmanned Aerial Vehicle

Parameter	Value
Wing Span	3.2 m
Length	1.7 m
Takeoff Weight	3.8 kg
Fuel Tank Capacity	8 L (6.3 kg)
Payload Capacity	5 kg
Min - Cruise - Max Speed	85 – 150 – 230 km/h
Operating Range	40 km
Max Climb Rate	16 m/s (at a speed of 140 km/h)

The UAV's flight test, as shown in Fig. 5, endured for approximately 15 minutes. The principal contributors to structural loading encompass take-off forces initiated by the catapult, dynamic forces incurred during flight maneuvers, and landing forces mitigated by a parachute. For the purposes of this investigation, only the dynamic load during flight maneuvers were taken into account. The highest velocity attained during the flight test was 88.9 m/s, accompanied by a peak acceleration of 10.2 g. Table 2 displays the 13 flight parameters documented during the flight test.

(a) Launching (b) In flight

Fig. 5 Flight test of the unmanned aerial vehicle [15].

B. Fibre Bragg Gratings Sensor Installment

The UAV was equipped with FBG sensors embedded in the wing skins. The locations of the 26 FBG strain sensors and 4 temperature sensors are illustrated in Fig. 6, situated on the upper right wing skin, lower right wing skin, upper left wing skin, and lower left wing skin, respectively, aligning with the wing span direction. Among them, 20 strain

Table 2 Recorded flight parameters

Parameter	Meaning	Unit	Frequency
GyrX, GyrY, GyrZ	X, Y, Z-axis angular velocity	deg/s	50 Hz
AccX, AccY, AccZ	X, Y, Z-axis linear acceleration	m/s^2	50 Hz
IAS	Indicated Airspeed	m/s	10 Hz
AOA	Angle of Attack	deg	10 Hz
SSA	Sideslip Angle	deg	10 Hz
PRESSURE	Atmospheric Pressure	MPa	10 Hz
Alt	Altitude	m	10 Hz
δ_l	Left Aileron Deflection	rad	10 Hz
δ_r	Right Aileron Deflection	rad	10 Hz

sensors were used to construct the load tracking model, while 6 FBG strain sensors in the lower skins on the left and right sides of the wing were used to test the prediction performance of the corresponding models.

As the Bragg reflection wavelength in the FBG sensors is influenced by both strain and temperature [15], the recorded strain is a composite of the aerodynamic load and the thermal strain induced by temperature variation. Four FBG sensors were used to measure the temperature for validation. The calibration coefficients of the 4 temperature FBG sensors to the 26 strain sensors were established during the laboratory test.

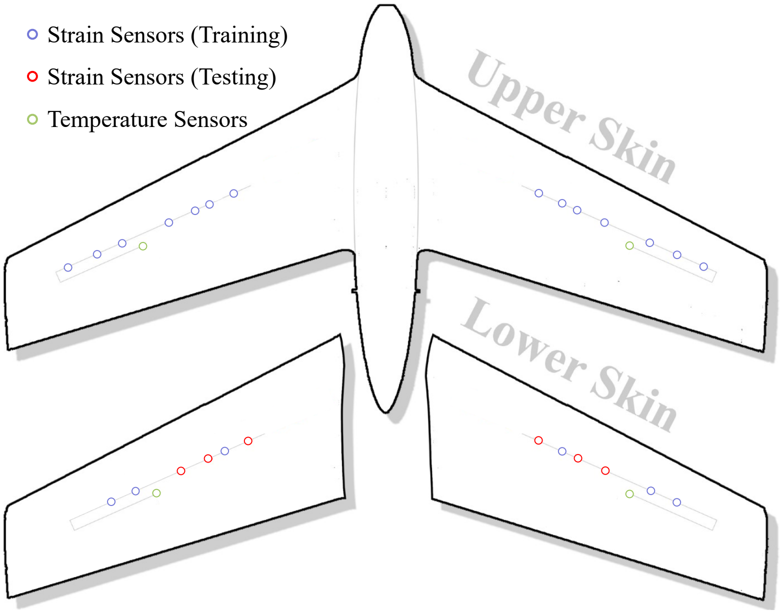

Fig. 6 Schematic layout of FBG sensors.

C. Laboratory Test for the Temperature Compensation of the UAV

In this study, a laboratory test was conducted to experimentally determine the temperature influence coefficients. Specifically, the UAV was divided into two independent sections (left and right wings), with a Negative Temperature

Coefficient (NTC) sensor installed on each wing. These sensors correlate temperature changes with strain variations while the structure remains unloaded. After calculating the temperature coefficients in the controlled laboratory environment, both the temperature shift and the equivalent load vector can be estimated using only the strain sensor data, without the need for additional sensors for compensation.

Data acquisition took place over two days. Part of the data was used to compute the influence coefficients, while the remaining data was used for result validation. Since temperature reconstruction cannot be directly validated during the flight test (due to the absence of NTC sensors in the same locations), the temperature reconstruction is verified on the ground by comparing the readings from the NTC sensors with the temperature values reconstructed through an inverse approach based on strain data, for the unloaded structure. Additional details can be found in Ref. [15]. The resulting influence coefficients are provided in Table 3.

Table 3 Calibrated temperature influence coefficients during the laboratory test

Sensor ID	Value	Sensor ID	value
1	25.3762	14	25.3762
2	25.3762	15	24.2914
3	25.3762	16	23.9233
4	25.3762	17	23.3982
5	25.3762	18	22.0771
6	25.3762	19	26.7598
7	25.3762	20	29.9992
8	17.8485	21	17.8485
9	17.8485	22	18.9596
10	17.8485	23	21.0582
11	17.8485	24	20.2657
12	17.8485	25	19.8096
13	17.8485	26	20.3011

D. Simulation Database Generation for the Inverse-direct Load Monitoring

In this subsection, leveraging the aerodynamic and structural models of the UAV, a simulation database is constructed for the inverse-direct load monitoring model.

The finite element model of the UAV was developed using ABAQUS software. The structural surfaces within the finite element model were primarily represented using shell elements, while internal load-bearing structures were modeled using 3D elements. The accuracy of the structural model has been verified in Ref. [21]. Additionally, a low-order 3D panel aerodynamic model was constructed using the PANUKL software. Furthermore, a program was adopted to extract the aerodynamic load distribution from the aerodynamic simulation result file and generate, through interpolation, a load mapping field suitable for ABAQUS finite element simulation. An example of the aerodynamic load distribution applied to the finite element model is depicted in Fig. 7.

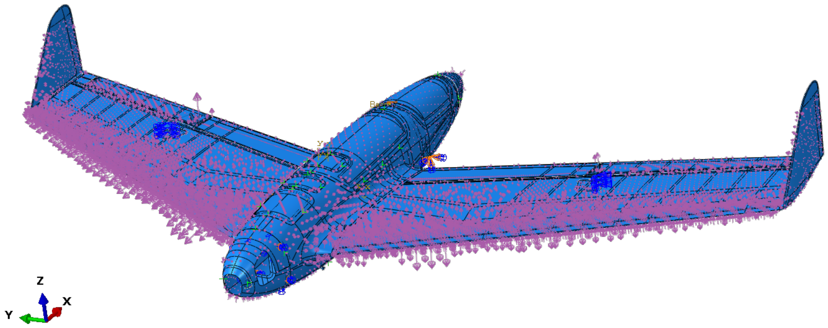

Fig. 7 Aerodynamic load distribution applied to the surface of the finite element model.

Table 4 delineates the specific eight flight parameters employed in the simulation, along with their respective ranges. 2000 samples are generated utilizing the Latin hypercube sampling method. The upper and lower limits are determined based on the range of measured flight data. Utilizing the PANUKL software in conjunction with batch simulation scripts, the aerodynamic load distributions were computed employing eight flight parameters as inputs.

Table 4 Flight parameters utilized in the simulation database generation

Parameter	Meaning	Lower Limit	Upper Limit	Unit
V	Indicated Airspeed	0.01	100	m/s
α	Angle of Attack	-10	15	deg
β	Sideslip Angle	-15	15	deg
p	Roll Rate	-0.1	0.1	rad/s
q	Pitch Rate	-0.1	0.1	rad/s
r	Yaw Rate	-0.02	0.02	rad/s
δ_l	Left Aileron Deflection	-10	20	rad
δ_r	Right Aileron Deflection	-10	20	rad

Following the acquisition of the aerodynamic load distribution for the 2000 samples, the loads are interpolated onto the outer surface of the finite element model in ABAQUS. Subsequently, structural simulation is executed through batch simulations. The load and deformation data pertaining to the entire aircraft, specific components, or regions of interest are retrieved from the ABAQUS output database files. Additionally, the virtual strain corresponding to the location of the real FBG strain sensors is extracted from the simulation database.

Ultimately, the acquired simulation database is represented as follows:

$$\mathcal{D}_{\text{sim}} = \left\{\mathbf{p}^{\text{sim}}, \mathbf{L}^{\text{sim}}, \mathbf{F}^{\text{sim}}, \varepsilon_{\text{FBG}}^{\text{sim}}\right\} \tag{11}$$

where $\mathbf{p}^{\text{sim}}$ represents the flight parameters in the simulation database, with a size of 2000×8; $\mathbf{L}^{\text{sim}}$ denotes the structural external load distribution data in the simulation database after interpolation, with a size of 2000×98858; and $\mathbf{F}^{\text{sim}}$

signifies the stress/strain/displacement distribution data in the simulation database. For each physical quantity of interest, it has a size of $2000 \times n_{\mathrm{node}}$ or $2000 \times n_{\mathrm{elem}}$, where n_{node} and n_{elem} are the number of nodes or elements in the region of interest, depending on whether the physical quantity is located at the node or at the centre of mass of the element. $\varepsilon_{\mathrm{FBG}}^{\mathrm{sim}}$ represents the virtual strain value for the location of the FBG strain sensor in the simulation database, with a size of 2000×20.

E. Dataset and Setting for the CNN-based Load Prediction Model of the UAV

In this study, the sampling frequency of strains is 1000 Hz, while the sampling frequency of the flight parameters is 50 Hz. Considering that high-frequency vibrations due to engine operation have little effect on the fatigue damage of the structure, and in order to establish temporal correspondence between flight parameters and strain measurements, the strain measurement data are downsampled to 50 Hz. Additionally, the UAV adopts catapult launching and recovery of the blocking net, resulting in a lower relationship between the measured data of the initial and end sections and the flight load in the flight test. Therefore, the initial and end segments were truncated in the flight parameters. Overall, the comprehensive dataset utilized in this study comprises a total of 800 seconds of flight test data, sampled at 50 Hz, resulting in 40,000 samples, encompassing measurements from 13 flight parameters, 26 FBG strain sensors, and 4 FBG temperature sensors.

For the data-driven load prediction model, the initial 20,000 samples were allocated for training, while the remaining 20,000 were designated for testing. Notably, the strain data employed in this study has undergone temperature compensation. This compensation allows the method to directly output prediction results after eliminating thermal strain, mitigating the impact of temperature changes on load prediction. Given the diverse amplitudes of flight parameters and strain measurements across different dimensions, the input and output data were initially uniformly scaled to the range of $[0, 1]$. Subsequently, the 20,000 samples were divided into sequences of equal length with a certain step size. In this case, the sequence length was set to 800, and the step size to 20, resulting in 961 time sequences. These sequences were then split into training and validation sets with an 80% to 20% ratio, as shown in Fig. 8. In order to effectively assess the model's generalization performance, the 961 training sequences were not randomized but arranged in the order they were collected during the flight test. Table 5 presents information on the preprocessed data.

Table 5 Dataset setting for the strain prediction model

Parameters	Value
Sample Count	20000
Window Length	800
Step Size	20
Training Set Count	768
Validation Set Count	193

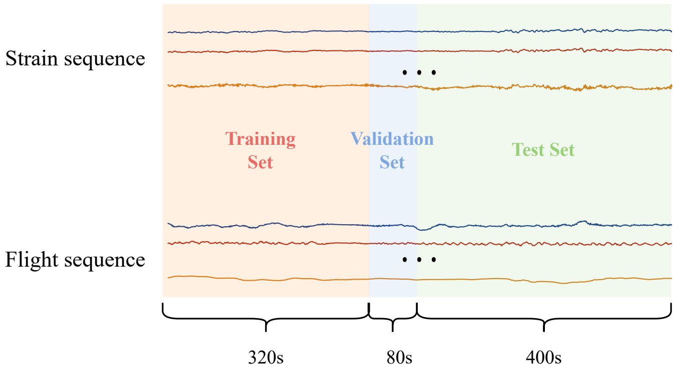

Fig. 8 Splitting of the dataset.

For the convolutional neural network, the convolutional kernel size is set to 5, the padding length is set to 2, and the stride is set to 1. These settings ensure that the size before and after the convolution remains unchanged. Specifically, the output of the convolutional module is of the same length as the input, facilitating the stacking of subsequent convolutional modules. The number of hidden neurons per layer is set to 64 for all networks. When the number of convolutional modules is set to 0, the fully connected neural network decomposes the sequence data into discrete sample data for processing. This aligns with the conventional approach of artificial neural networks.

IV. Load Tracking Results on the Unmanned Aerial Vehicle

A. Load Tracking of the UAV with Strain Measurements and the Improved Inverse-Direct Method

In this subsection, the load monitoring result with the improved inverse-direct method is presented, compared with the method without temperature compensation. The model is constructed with the simulation database and validated with the flight test data. The method's performance is compared with strain measurements from the six test sensor locations. The selection of an optimal number of principal components is made after a thorough comparison of the impacts of varying the number of principal components on the inversion results throughout the model construction process, as shown in Section V.A.1.

In Fig. 9, the predicted strains for the FBG sensors at the six test locations are visualized. Notably, the strain predictions, incorporating the temperature compensation strategy, exhibit a close alignment with the measured results. Conversely, without temperature compensation, significant disparities emerge, primarily in the estimated aerodynamic loads, where inaccuracies stem from the interference of thermal strains in the measured strains. Consequently, in the subsequent strain prediction, these inaccuracies in load input contribute to noticeable deviations in the predicted strains.

Moving to Fig. 10, we present a comparative analysis between methods that consider temperature compensation and those that do not, with the thermal strain values removed. A notable distinction between the estimated and measured values becomes apparent, particularly in the initial quarter of the six test locations. Fig. 11 offers a detailed examination

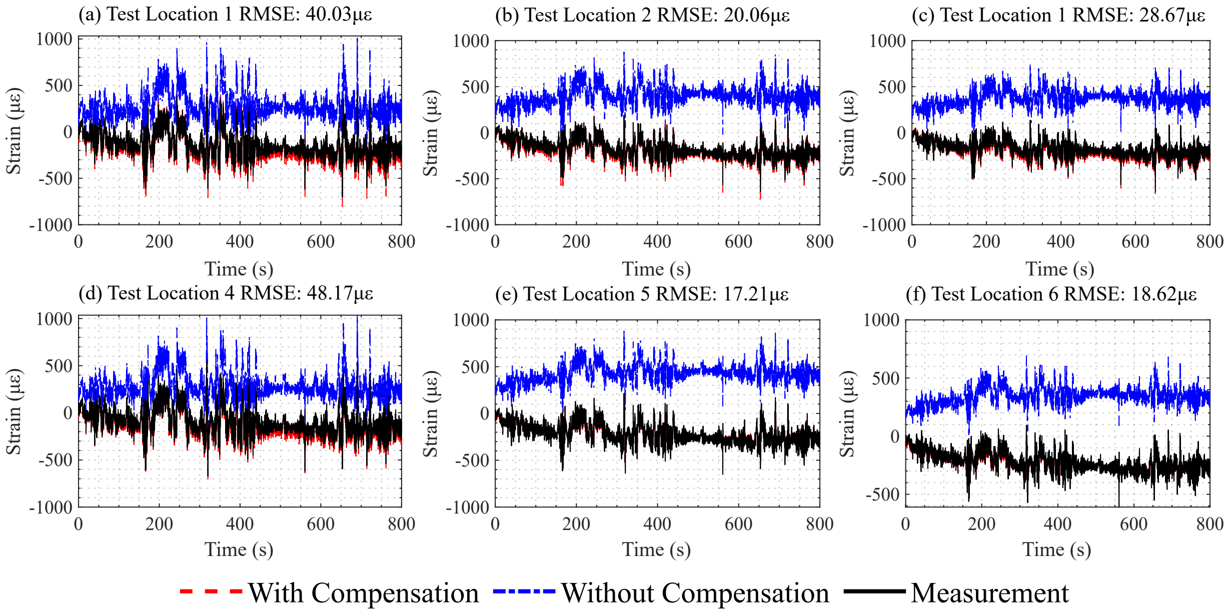

Fig. 9 Inversed strain at test positions superimposed with thermal strain.

of the disparity between inverted and measured thermal strain values at six distinct test locations. The overall trajectory of the inverted thermal strains, when compared to the estimated values from temperature FBGs, maintains consistency throughout the entire flight. Notably, the temperature undergoes a descent following the initiation of the flight, stabilizing into a gradual trend as the aircraft reaches higher altitudes.

In contrast to measurements, the estimated thermal strain derived from the calibration matrix exhibits a more rapid change at the beginning of the test. This phenomenon can be attributed to the characteristics of the FBG sensors employed for temperature strain measurements. As explained in [15], these sensors were attached to a relatively thick layer of anti-vibration foam to capture the thermal effects of strains, resulting in a delayed response to external temperature variations. Consequently, during the initial stages of the flight, when the structure had not yet reached thermal equilibrium, the measurements in Fig. 10 were susceptible to errors, thereby diminishing the accuracy of the strain reconstruction.

Fig. 12 illustrates the comparison between simulation-based predictions, the inverse-direct load monitoring method presented in [15], and our proposed improved inverse-direct load monitoring method. The simulation-based prediction utilizes the aerodynamic and structural reduced-order models trained by the simulation database, with flight parameters as inputs. It is evident that our proposed approach outperforms existing methods, primarily attributed to the utilization of reduced-dimensional aerodynamic loads instead of the equivalent load set as proposed in [15]. Notably, the average error of the six sensors is reduced from 38.5241 $\mu\varepsilon$ to 31.0617 $\mu\varepsilon$, representing a significant 19.4% reduction in error. Conversely, the simulation-based prediction yields a larger error, primarily due to limitations in the fidelity of both the aerodynamic and structural models.

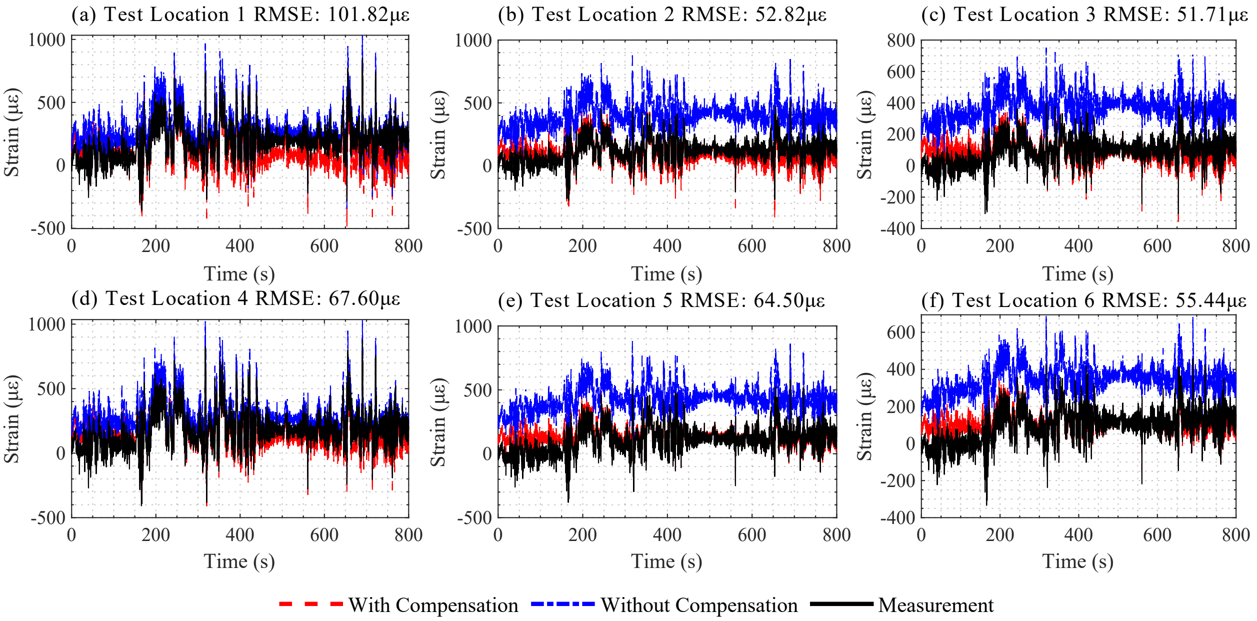

Fig. 10 **Inversed strain at test positions without thermal strains.**

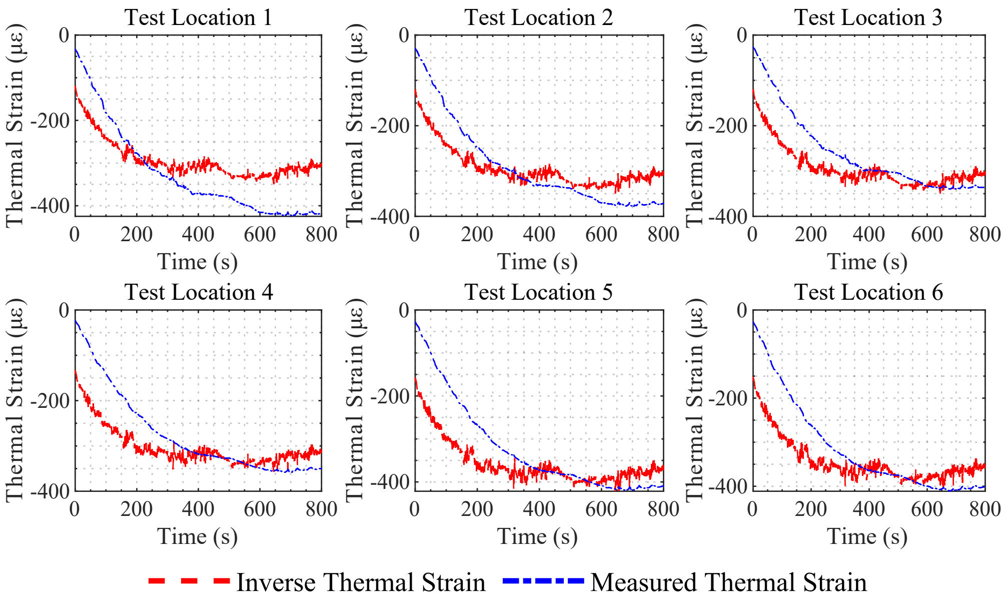

Fig. 11 **Comparison of thermal strain at test locations.**

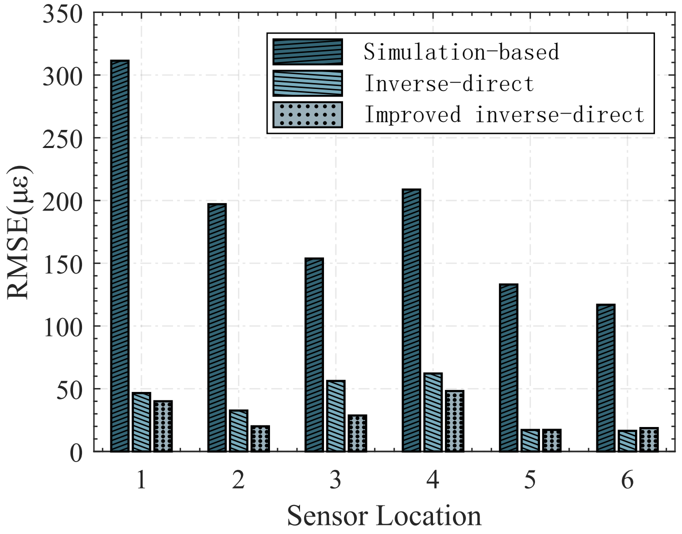

Fig. 12 Comparison of strain prediction errors at test sensor positions.

It is crucial to underscore that the aerodynamic load values obtained from the load inversion results may not necessarily represent the true aerodynamic load distribution. As evident from both the inverse and direct processes, the inverse load estimation model primarily accounts for the proportionality between strain sensor measurements and strains in other parts of the structure. Even if there are discrepancies between the results of the finite element model and the actual conditions due to factors such as material parameters, the accuracy of the prediction results is enhanced as long as this proportionality closely aligns with the realistic structure.

Indeed, the reliability of prediction results can be compromised if the model itself has limitations. For instance, if the model fails to consider nonlinearities or inaccurately defines component connection relationships, ensuring the accuracy of prediction results becomes a challenging task which needs to be addressed in future studies.

B. Comparison of the Strain Prediction of the UAV using the Flight Parameters

In this subsection, the predictive performance of the CNN model is compared with that of the LSTM and Fully-Connected Neural Network (FNN) models, as shown in Table 6. For consistency, the number of hidden neurons per layer is set to 64 for both the LSTM and FNN models. The LSTM model consists of six layers to match the number of parameters in the CNN model, while the FNN model only contains two layers as a baseline. The training and validation losses represent the normalized loss functions for the respective datasets, and the strain error for the test set is evaluated using the Root Mean Square Error (RMSE), calculated from the strain measurements.

The prediction results for the test samples from the second half of the flight test at the first test sensor location are presented in Fig. 13. Two sources of model prediction errors are observed in this case: the first arises from the deviation of the prediction results from the overall trend of the actual measurements, manifesting as a noticeable offset. The

Table 6 Comparison of performance for the proposed CNN-based model with the LSTM-based and FNN-based model

Network	Training Loss	Validation Loss	Test Error ($\mu\varepsilon$)
CNN	0.0064	0.0132	26.02
LSTM	0.0227	0.0589	59.03
FNN	0.0177	0.0416	52.19

second is due to overly smooth predictions that fail to capture high-frequency components, which resemble a smoothing or filtering effect on real values. As shown in Fig. 13a, the CNN effectively captures high-frequency variations in strain, with the predicted results closely aligning with the measured values and exhibiting oscillations only in specific regions. In contrast, the LSTM model in Fig. 13b produces smoother results, with deviations observed in certain regions, indicating that the primary source of error for the LSTM network is the second factor. The FNN results in Fig. 13c are similarly smooth but show some bias.

In general, a traditional fully connected neural network can be viewed as a low-pass filter. Different layers of the network learn features at varying levels of abstraction. The lower layers typically capture fundamental features, while the higher layers progressively extract more abstract and complex features. This hierarchical feature extraction process resembles low-pass filtering, which smooths out the high-frequency components of a signal, allowing the network to focus on the overall trend. In the case of recurrent neural networks, despite LSTM's improved handling of short-term dependencies compared to classical RNNs, the results tend to emphasize global trends, resulting in the loss of local high-frequency information. This explains the observed performance degradation when LSTM modules are added to the network, with further decline as the number of LSTM modules increases.

Conversely, CNNs are typically more effective at capturing high-frequency features. CNNs share weights across spatial dimensions, enabling them to capture local patterns and fine details. In image processing tasks, CNNs excel at detecting high-frequency features, such as edges and textures, even when these components are nearly imperceptible to humans [32]. Similarly, in time series data with rapidly changing patterns, CNNs efficiently capture these variations. The impact of the number of CNN and FNN layers on the performance is further explored in Section V.B. It is worth noting that employing a multi-flight dataset is desired in future works to encompass a broader range of maneuvers and environmental conditions, which would enhance the CNN model's ability to learn diverse relationships and reduce the risk of overfitting.

C. In-service Load Tracking and Deformation Prediction of the UAV

In this subsection, we first present the load tracking results at six test sensor locations to compare performance with the measurements. Subsequently, we demonstrate the proposed method's capability to predict the full-field load and deformation distribution, underscoring its advantages in the development of an airframe digital twin. This advancement

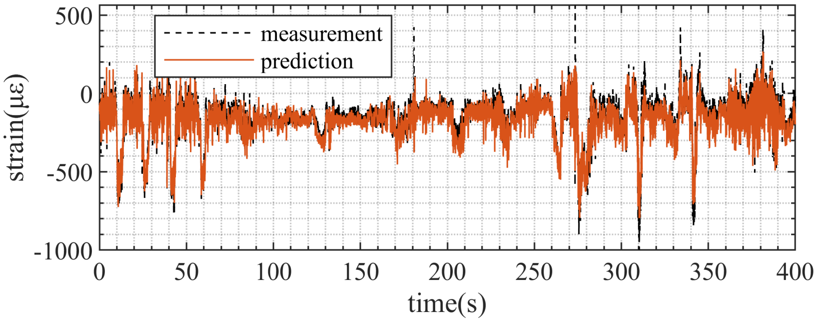

(a) CNN

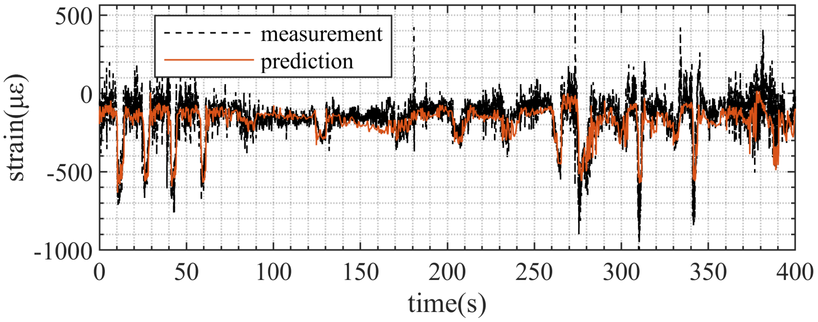

(b) LSTM

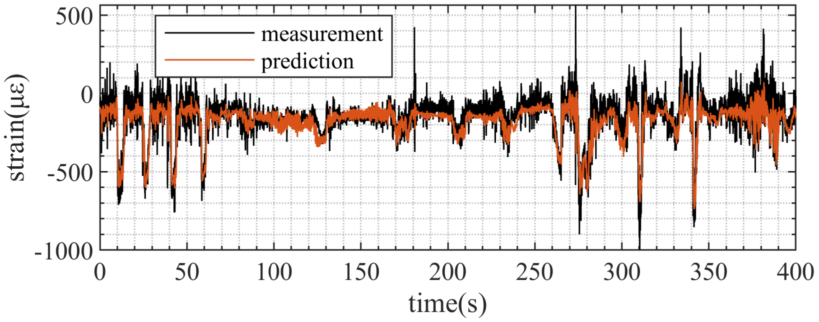

(c) FNN

Fig. 13 Comparison of strain predictions for the proposed CNN-based model with the LSTM-based and FNN-based model at the first test sensor position.

is crucial for understanding damage evolution and enabling condition-based maintenance.

Fig. 14 depicts the result of flight load tracking derived from the inverse-direct load monitoring model, with the predicted strain utilizing the CNN-based strain prediction model as input. As the CNN model was trained using data from the first half of the flight test, only results from the latter half are presented herein. It can be seen that the fusion of deep learning and inverse-direct load monitoring, as employed in this section, yields results comparable to the original load monitoring method, thus affirming the efficacy of the proposed approach.

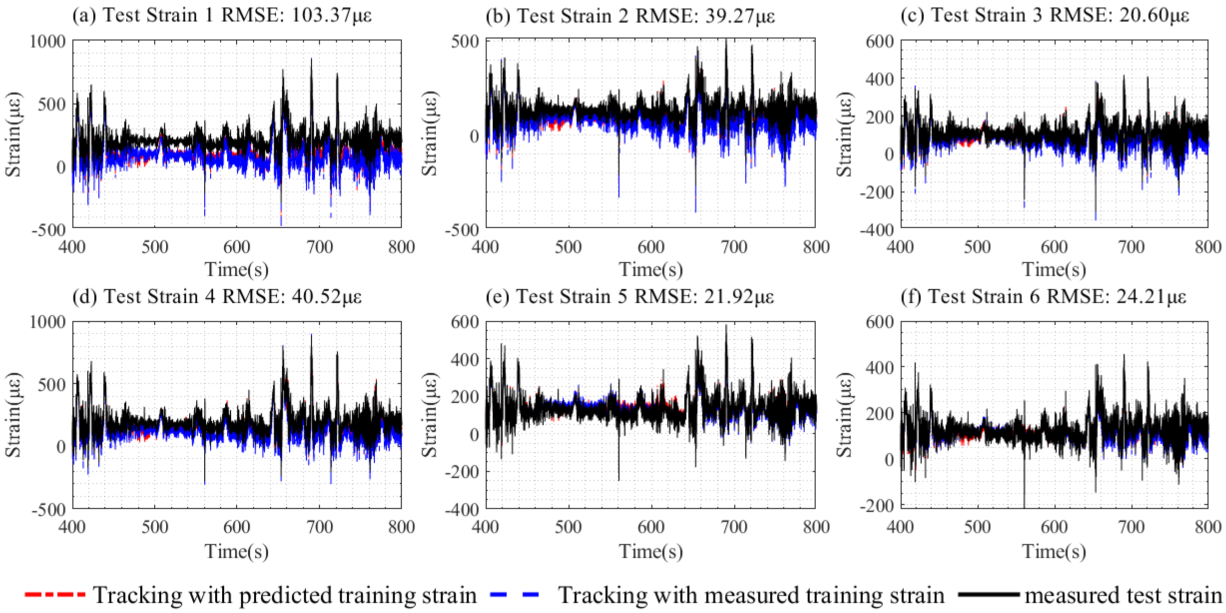

Fig. 14 In-service load tracking results on the six test sensor locations.

Notably, this method utilizes solely flight data, akin to the aerodynamic/structural reduced-order prediction method; however, it outperforms the latter in terms of prediction accuracy. This improvement may be attributed to the incorporation of acceleration data in the flight parameter dataset and the establishment of a mapping relationship between flight parameters and real strain. Consequently, the proposed method demonstrates superior performance compared to the aerodynamic/structural reduced-order prediction. To substantiate these findings, further validation is imperative, encompassing multiple sets of flight tests and diverse aircraft of the same type in future research.

As the performance of load tracking is validated at the test sensor locations, the advantages of the proposed method for full-field load and deformation distribution are further illustrated. It is worth mentioning that full-field prediction can be conducted in real time for the aircraft during flight. Fig. 15 presents the aerodynamic pressure, von Mises stress, von Mises strain, and z-direction displacement distributions at two selected timestamps, and the corresponding flight parameters of the two cases are shown in Table 7. There is a slight difference in the pressure distribution between the two cases, while the displacement distributions exhibit substantial differences. Differences in the stress and strain distributions are also visible.

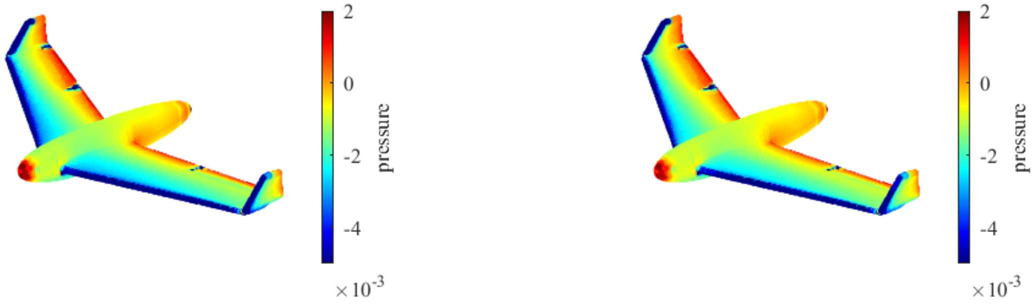

(a) Pressure of the first case **(b) Pressure of the second case**

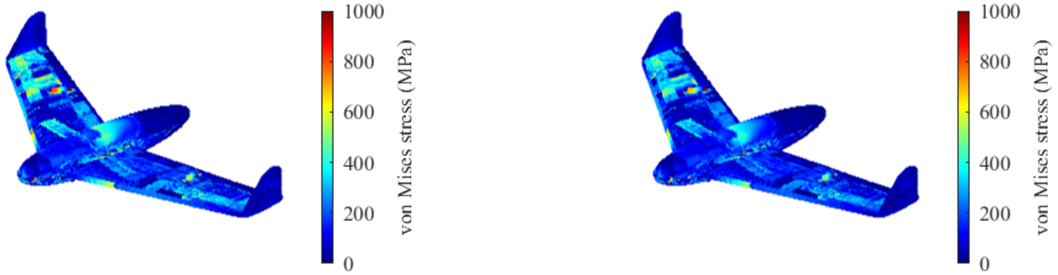

(c) von Mises Stress of the first case **(d) von Mises stress of the second case**

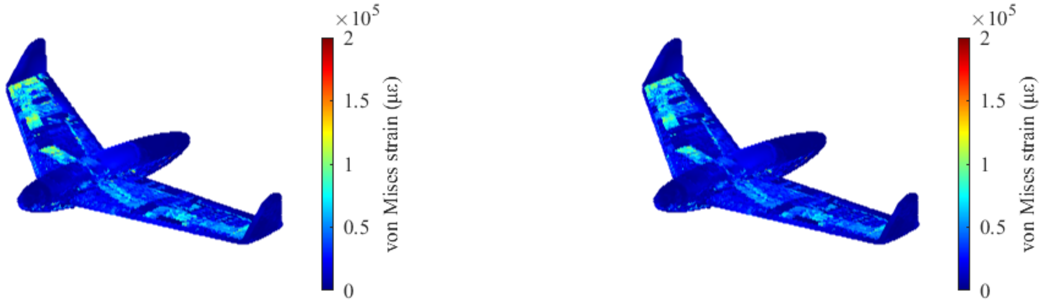

(e) von Mises strain of the first case **(f) von Mises strain of the second case**

(g) U3 of the first case **(h) U3 of the second case**

Fig. 15 Full-field deformation prediction with flight parameters as input at two different timestamps.

Table 7 The typical flight parameters at the two selected timestamp

Case	AOA (deg)	Speed (m/s)	Left aileron angle (deg)	Right aileron angle (deg)
1	2.0975	43.6228	-12.2143	-0.3872
2	2.0370	50.8381	-14.0136	10.6797

Since the deformations are predicted, their accuracy is difficult to quantify and is thus analyzed qualitatively. It can be observed that for similar angles of attack in both cases, the displacement in the second case is larger than in the first case due to the higher airspeed. Additionally, because the right aileron angle is greater than the left in both cases, the stresses, strains, and displacements on the right side of the wing are greater than those on the left. Furthermore, the larger difference in aileron angle between the two sides in the second case results in more pronounced deformation differences.

Finally, it is important to note that the sensors in this study were installed at some distance from the ailerons. Although aileron deflection affects the strain at these sensor locations and there is a correlation between aileron loads and strain measurements, the existing scheme is less effective in capturing this correlation compared to directly placing sensors near the ailerons. Consequently, the aerodynamic loads obtained from the inversion do not sufficiently capture the variations in aileron loads, as shown in Figs. 15a and 15b, which also impacts the prediction of structural deformation. Further optimization of sensor installation locations is needed in subsequent studies.

V. Effect of Sensor Placement and Model Parameter on the Method Performance

In this section, several factors that affect the performance of the proposed in-service load tracking framework are discussed. In Section V.A, the effect of the number of sensors and principal components on the improved inverse-direct load monitoring model is provided, while in Section V.B, the variation of the network structures on the data-driven strain prediction model are considered.

A. Effect of the Number of Sensors and Principal Components on the Load Tracking Results

In the proposed improved inverse-direct load monitoring method, the number of principal components would affect the reduced-dimensional representation of the aerodynamic load, thereby impacting the load monitoring result.

1. Effect of the number of principal components on the inverse and direct model

Fig. 16 demonstrates the model errors and correlation coefficients for different numbers of principal components when constructing the inverse and direct models based on the simulation database. The test locations here refer to the six test strain sensors. It can be seen that when the number of principal components increases from 3 to 6, the prediction errors of the two models decrease rapidly, while the correlation coefficients increase quickly. After the number of principal components is greater than 6, the trend of decreasing model errors and increasing correlation coefficients decreases, which confirms the results of the analysis of the effect of the number of principal components on the reduced-dimensional aerodynamic loads in the previous section.

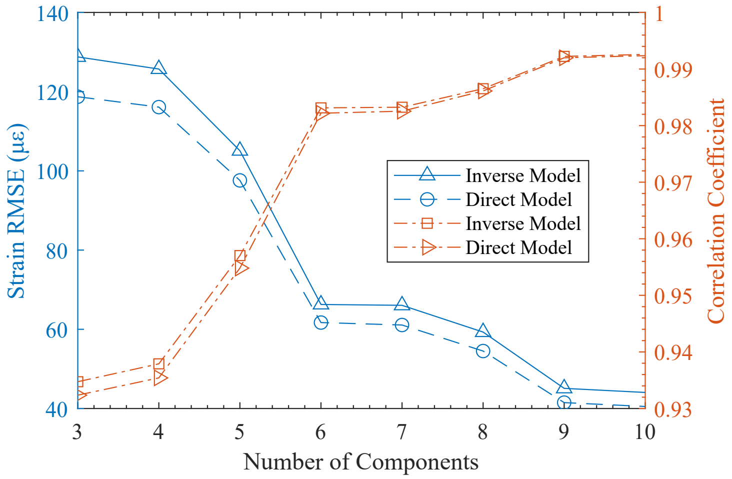

Fig. 16 Effect of the number of principal components on the performance of the load inversion model and deformation prediction model.

Additionally, the influence of the number of principal components on the condition number of the calibration matrix is analyzed, as illustrated in Fig. 17. The condition number of the calibration matrix experiences a significant escalation when the number of principal components exceeds 6. The large condition numbers can render the load inversion results susceptible to the impact of measurement noise, thereby compromising the stability of the inversion outcomes. Consequently, guided by the preceding analysis, we opt for six principal components to characterize the reduced-order loads. This decision stems from a balance between model training accuracy and the stability of practical predictions.

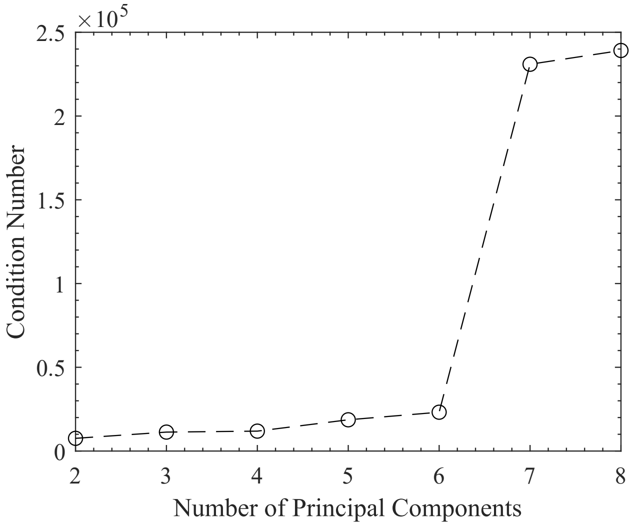

Fig. 17 Effect of the number of principal components on the condition number of the calibration matrix.

2. Impact of the quantity of principal components and sensors on the load tracking result

A comparison of the effects of different sensor numbers on the tracking result is provided, offering insights into the sensitivity of the model to variations in the quantity of sensors. Given that the sensor layout was fixed and cannot be changed, a strategy was employed to mitigate the potential bias introduced by specific sensor selections. Specifically, eight sequences of random numbers, each comprising a length of 20, were generated. For each sequence, strain measurements from a designated number of sensors were sequentially chosen as inputs. Subsequently, the load inversion algorithm was executed, and the computed errors were averaged. This approach serves as a means to simulate the reduction of the sensor numbers. The effect of the number of principal components is also provided for comparison.

From Fig. 18a, it can be observed that when the number of principal components is unchanged, the test error of the inverse model generally increases with the decrease in the number of sensors. This indicates that the number of sensors should be increased as much as possible for practical use while meeting the requirements of airworthiness, weight, and cost. However, it should be emphasized that the sensor layout was not further optimized when reducing the number of sensors, which also affects the results and needs to be considered in future work.

Observing the variation of the number of principal components in Fig. 18a, it is evident that when the number of sensors is large, the test error of the inverse model decreases and then increases with the increase in the number of reduced-order principal components. This may occur because the increase in the number of principal components can better characterize the aerodynamic load distribution. However, due to correlations between the strain sensors, the condition number of the calibration matrix of the inverse model may become larger when the number of principal components is too high, as demonstrated in Fig. 17.

Different sensor positions can also have an effect on the results of load inversion. Fig. 18b presents the standard deviation of the results obtained with eight different choices of sensor locations for each case of the number of sensors. When the number of sensors is less than 15, the standard deviation is larger, suggesting that with a smaller number of sensors, the location of the sensors has a greater impact on the prediction results, and finer layout optimization is needed to reduce the uncertainty of the prediction results.

In Fig. 18c, the effect of the number of sensors on the condition number is further considered. It can be seen that when the number of principal components is greater than 6, the condition number tends to increase with a smaller number of sensors. As the matrix approaches illness, the test error becomes susceptible to measurement noise.

B. Performance Comparison of Data-driven Load Prediction Models with Different Network Structures

In this subsection, different network structures with different number of CNN layers and FNN layers are compared to find an optimal network structure for the strain prediction model.

With regard to the effect of the CNN layers, from Fig. 19, it is observed that both the training set loss and the validation set loss initially decrease. When the number of CNN layers exceeds 5, the network errors exhibit a significant

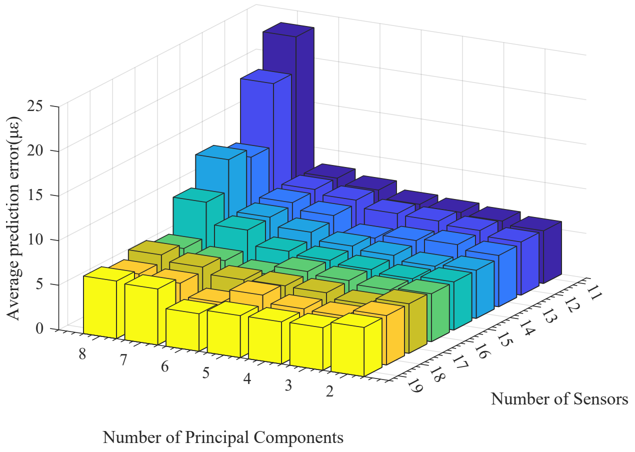

(a) Prediction error

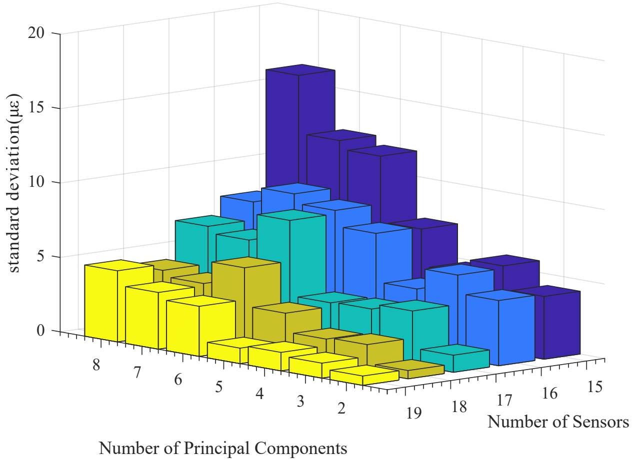

(b) Standard deviation

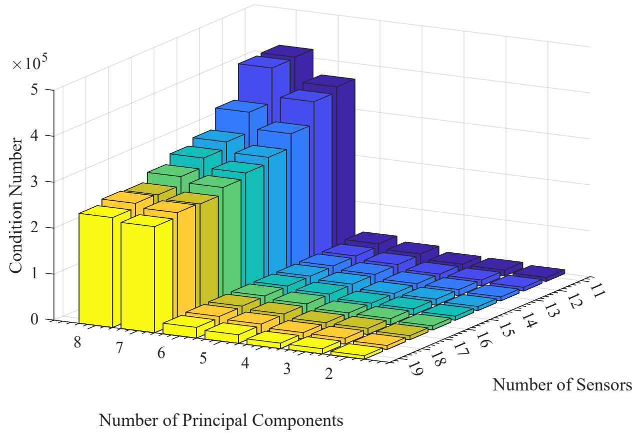

(c) Condition number of the calibration matrix

Fig. 18 Effect of the number of sensors and principal components on the load tracking.

reduction, especially in the validation set loss, indicating improved learning of features describing strain changes with flight parameters. However, the error shows a slight increase after the number of CNN layers exceeds 9, with a subsequent decrease at 14 layers. This suggests the potential for overfitting with too many layers. Therefore, in subsequent studies, the number of CNN layers was set to 9.

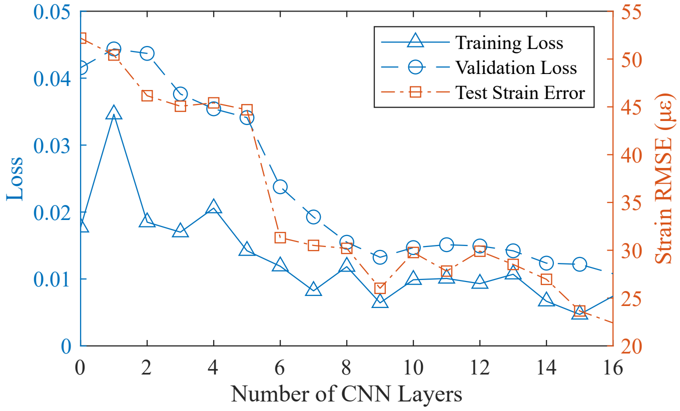

Fig. 19 Comparison of strain prediction results with different number of CNN layers.

Furthermore, it is notable that the overall trend of the validation set loss function is larger than that of the training set loss. Additionally, the validation set loss exhibits a similar trend to the test set strain prediction error. This discrepancy arises from the fact that the samples in the training and validation sets in this study correspond to different stages of the flight test. Consequently, the obtained loss function values better characterize the generalisation performance of the model. However, due to the proximity of the validation set samples to the training set samples compared to the test set samples, the local variation in the validation set loss does not precisely mirror the test set error.

The impact of different numbers of fully connected layers on the performance of the convolutional neural network is further examined, as illustrated in Fig. 20. It is observed that the training set loss gradually decreases with an increase in the number of fully connected layers. However, the validation set loss and the test set strain prediction error oscillate after the number of fully connected layers reaches 2. This oscillation suggests a potential overfitting condition when the number of fully connected layers is too high. Consequently, for this study, the number of fully connected layers was selected as 2.

VI. Conclusion

In this study, an in-service load tracking method tailored to the flight load acquisition requirements of the airframe digital twin is proposed. This method integrates available flight and strain data from flight tests with aerodynamic and structural simulation models, resulting in an in-service flight load tracking framework. A UAV with a 3.2-meter wingspan is utilized to validate the proposed in-service load tracking approach using real flight data.

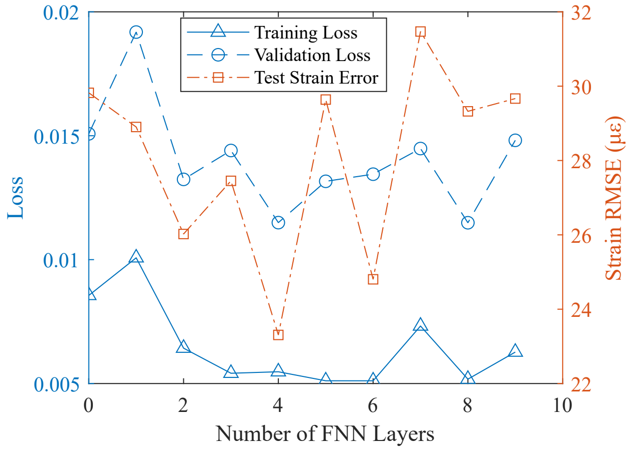

Fig. 20 Comparison of strain prediction results with different number of FNN layers.

First, an improved inverse-direct load monitoring method is proposed. This method utilizes reduced-dimensional aerodynamic load representation instread of discrete section load, and adopted a temperature reconstruction and compensation strategy, resulting in superior prediction accuracy compared to section load-based methods. The approach exhibits a 19.4% reduction in error across six test strain sensors.

Then, a deep learning-based flight parameter-strain prediction model is constructed using the flight parameter and strain data during the flight test. It reveals the effectiveness of convolutional neural networks in predicting high-frequency signals in strain history, compared with long short-term memory network and full-connect neural network. In the service stage, the convolutional neural network is employed to predict load-related strain corresponding to the position of FBG sensors using flight parameters as inputs.

Finally, an in-service flight load tracking framework is proposed. The data-driven load prediction model is combined with the inverse-direct method to achieve full-field load and deformation tracking during the service stage, without the need for additional strain sensors.

However, it is crucial to note that the methodology validation in this study relies on a single-flight test. Employing multiple flight tests in future studies would offer clear benefits: A multi-flight dataset would encompass a broader range of maneuvers and environmental conditions, enhancing the machine learning model's ability to learn diverse relationships and reducing the risk of overfitting. Moreover, cross-validation across distinct flight instances would yield more reliable estimates of model performance and uncertainty, thereby improving both generalizability and robustness. Finally, we are also exploring the extension of this framework to nonlinear scenarios—such as nonlinear aeroelastic aircraft—to further broaden its applicability.

Acknowledgments

This work has been developed based on the results from SAMAS (SHM application to Remotely Piloted Aircraft Systems) project, a Category B project coordinated by the European Defense Agency (EDA) and financed by two nations, Italy and Poland. The project consortium includes the following parties: Italy (Politecnico di Milano, Leonardo Società per azioni) and Poland (Instytut Techniczny Wojsk Lotniczych — Air Force Institute of Technology, Military Aviation Works No. 1).

References

[1] De Jonge, J. B., "Monitoring Load Experience of Individual Aircraft," *Journal of Aircraft*, Vol. 30, No. 5, 1993, pp. 751–755. https://doi.org/10.2514/3.46407.

[2] Tuegel, E. J., Ingraffea, A. R., Eason, T. G., and Spottswood, S. M., "Reengineering Aircraft Structural Life Prediction Using a Digital Twin," *International Journal of Aerospace Engineering*, Vol. 2011, 2011, p. 154798. https://doi.org/10.1155/2011/154798.

[3] Glaessgen, E., and Stargel, D., "The Digital Twin Paradigm for Future NASA and U.S. Air Force Vehicles," *53rd AIAA/ASME/ASCE/AHS/ASC Structures, Structural Dynamics and Materials Conference*, American Institute of Aeronautics and Astronautics, Honolulu, Hawaii, 2012, p. 1818. https://doi.org/10.2514/6.2012-1818.

[4] Li, C., Mahadevan, S., Ling, Y., Choze, S., and Wang, L., "Dynamic Bayesian Network for Aircraft Wing Health Monitoring Digital Twin," *AIAA Journal*, Vol. 55, No. 3, 2017, pp. 930–941. https://doi.org/10.2514/1.J055201.

[5] Liao, M., Renaud, G., and Bombardier, Y., "Airframe Digital Twin Technology Adaptability Assessment and Technology Demonstration," *Engineering Fracture Mechanics*, Vol. 225, 2020, p. 106793. https://doi.org/10.1016/j.engfracmech.2019.106793.

[6] Sisson, W., Karve, P., and Mahadevan, S., "Digital Twin Approach for Component Health-Informed Rotorcraft Flight Parameter Optimization," *AIAA Journal*, Vol. 60, No. 3, 2022, pp. 1923–1936. https://doi.org/10.2514/1.J060770.

[7] Gao, B., Ye, Y., Pan, X., Yang, Q., Xie, W., Meng, S., and Huo, Y., "A Dynamic Reliability Prognosis Method For Reusable Spacecraft Mission Planning Based On Digital Twin Framework," *ASCE-ASME J Risk and Uncert in Engrg Sys Part B Mech Engrg*, Vol. 9, No. 4, 2023, p. 041102. https://doi.org/10.1115/1.4063297.

[8] Liu, Y., Wang, L., Li, M., and Wu, Z., "A Distributed Dynamic Load Identification Method Based on the Hierarchical-Clustering-Oriented Radial Basis Function Framework Using Acceleration Signals under Convex-Fuzzy Hybrid Uncertainties," *Mechanical Systems and Signal Processing*, Vol. 172, 2022, p. 108935. https://doi.org/10.1016/j.ymssp.2022.108935.

[9] Zhou, X., He, S., Dong, L., and Atluri, S. N., "Real-Time Prediction of Probabilistic Crack Growth with a Helicopter Component Digital Twin," *AIAA Journal*, Vol. 60, No. 4, 2022, pp. 2555–2567. https://doi.org/10.2514/1.J060890.

[10] Gao, J., Wang, S., Zhang, C., Chen, R., Zhang, Y., Zhang, Y., and Mu, R., “Energy-Based Multi-Axial Fatigue Prediction for Tubular Structures under Non-Proportional Loading,” *International Journal of Fatigue*, Vol. 197, 2025, p. 108897. https://doi.org/10.1016/j.ijfatigue.2025.108897.

[11] Zhou, X., Sbarufatti, C., Giglio, M., Dong, L., and Atluri, S. N., “Copula-Based Collaborative Multistructure Damage Diagnosis and Prognosis for Fleet Maintenance Digital Twins,” *AIAA Journal*, Vol. 61, No. 10, 2023, pp. 4735–4740. https://doi.org/10.2514/1.J063105.

[12] Zhao, F., Zhou, X., Wang, C., Dong, L., and Atluri, S. N., “Setting Adaptive Inspection Intervals in Helicopter Components, Based on a Digital Twin,” *AIAA Journal*, Vol. 61, No. 6, 2023, pp. 2675–2688. https://doi.org/10.2514/1.J062222.

[13] Chen, R., Wang, S., Zhang, C., Dui, H., Zhang, Y., Zhang, Y., and Li, Y., “Component Uncertainty Importance Measure in Complex Multi-State System Considering Epistemic Uncertainties,” *Chinese Journal of Aeronautics*, 2024. https://doi.org/10.1016/j.cja.2024.05.024.

[14] Lu, Y., Wang, S., Zhang, C., Chen, R., Dui, H., Mazurkiewicz, D., and Zhang, Y., “A Dynamic Imperfect Inspection-Based Maintenance Optimization Considering Dependent Competing Failure,” *Measurement*, 2025, p. 117470. https://doi.org/10.1016/j.measurement.2025.117470.

[15] Colombo, L., Sbarufatti, C., Zielinski, W., Dragan, K., and Giglio, M., “Numerical and Experimental Flight Verifications of a Calibration Matrix Approach for Load Monitoring and Temperature Reconstruction and Compensation,” *Aerospace Science and Technology*, Vol. 118, 2021, p. 107074. https://doi.org/10.1016/j.ast.2021.107074.

[16] Reed, S. C., “Indirect Aircraft Structural Monitoring Using Artificial Neural Networks,” *The Aeronautical Journal*, Vol. 112, No. 1131, 2008, pp. 251–265. https://doi.org/10.1017/S0001924000002190.

[17] Gockel, B., Tudor, A., Brandyberry, M., Penmetsa, R., and Tuegel, E., “Challenges with Structural Life Forecasting Using Realistic Mission Profiles,” *53rd AIAA/ASME/ASCE/AHS/ASC Structures, Structural Dynamics and Materials Conference*, American Institute of Aeronautics and Astronautics, Reston, 2012, p. 1813. https://doi.org/10.2514/6.2012-1813.

[18] Colombo, L., Todd, M. D., Sbarufatti, C., and Giglio, M., “On Statistical Multi-Objective Optimization of Sensor Networks and Optimal Detector Derivation for Structural Health Monitoring,” *Mechanical Systems and Signal Processing*, Vol. 167, 2022, p. 108528. https://doi.org/10.1016/j.ymssp.2021.108528.

[19] Liu, Y., and Wang, L., “Multiobjective-Clustering-Based Optimal Heterogeneous Sensor Placement Method for Thermo-Mechanical Load Identification,” *International Journal of Mechanical Sciences*, Vol. 253, 2023, p. 108369. https://doi.org/10.1016/j.ijmecsci.2023.108369.

[20] Colombo, L., Oboe, D., Sbarufatti, C., Cadini, F., Russo, S., and Giglio, M., “Shape Sensing and Damage Identification with iFEM on a Composite Structure Subjected to Impact Damage and Non-Trivial Boundary Conditions,” *Mechanical Systems and Signal Processing*, Vol. 148, 2021, p. 107163. https://doi.org/10.1016/j.ymssp.2020.107163.

[21] Colombo, L., Sbarufatti, C., Bosco, L. D., Bortolotti, D., Dziendzikowski, M., Dragan, K., Concli, F., and Giglio, M., "Numerical and Experimental Verification of an Inverse-Direct Approach for Load and Strain Monitoring in Aeronautical Structures," *Structural Control and Health Monitoring*, Vol. 28, No. 2, 2021, p. e2657. https://doi.org/10.1002/stc.2657.

[22] Coates, C. W., and Thamburaj, P., "Inverse Method Using Finite Strain Measurements to Determine Flight Load Distribution Functions," *Journal of Aircraft*, Vol. 45, No. 2, 2008, pp. 366–370. https://doi.org/10.2514/1.21905.

[23] Lee, H., Cho, H., and Park, S., "Review of the F-16 Individual Aircraft Tracking Program," *Journal of Aircraft*, Vol. 49, No. 5, 2012, pp. 1398–1405. https://doi.org/10.2514/1.C031692.

[24] Ostrom, J., "Inverse Flight Simulation for a Fatigue Life Management System," *AIAA Modeling and Simulation Technologies Conference and Exhibit*, American Institute of Aeronautics and Astronautics, Reston, 2005, p. 6212. https://doi.org/10.2514/6.2005-6212.

[25] Kiranyaz, S., Avci, O., Abdeljaber, O., Ince, T., Gabbouj, M., and Inman, D. J., "1D Convolutional Neural Networks and Applications: A Survey," *Mechanical Systems and Signal Processing*, Vol. 151, 2021, p. 107398. https://doi.org/10.1016/j.ymssp.2020.107398.

[26] Dou, Z., Gao, C., Zhang, W., and Tao, Y., "Nonlinear Aeroelastic Prediction in Transonic Buffeting Flow by Deep Neural Network," *AIAA Journal*, Vol. 61, No. 6, 2023, pp. 2412–2429. https://doi.org/10.2514/1.J061946.

[27] Zhang, R., Chen, Z., Chen, S., Zheng, J., Büyüköztürk, O., and Sun, H., "Deep Long Short-Term Memory Networks for Nonlinear Structural Seismic Response Prediction," *Computers & Structures*, Vol. 220, 2019, pp. 55–68. https://doi.org/10.1016/j.compstruc.2019.05.006.

[28] Gulgec, N. S., Takáč, M., and Pakzad, S. N., "Structural Sensing with Deep Learning: Strain Estimation from Acceleration Data for Fatigue Assessment," *Computer-Aided Civil and Infrastructure Engineering*, Vol. 35, No. 12, 2020, pp. 1349–1364. https://doi.org/10/ghkdpv.

[29] Levinski, O., Conser, D., Mouser, C., Koschel, S., Carrese, R., Candon, M., and Marzocca, P., "An Innovative High-Fidelity Approach to Individual Aircraft Tracking," *AIAA Scitech 2020 Forum*, American Institute of Aeronautics and Astronautics, Orlando, 2020. https://doi.org/10.2514/6.2020-1647.

[30] Guo, Y., Mahadevan, S., Matsumoto, S., Taba, S., and Watanabe, D., "Investigation of Surrogate Modeling Options with High-Dimensional Input and Output," *AIAA Journal*, Vol. 61, No. 3, 2023, pp. 1334–1348. https://doi.org/10.2514/1.J061901.

[31] Bhaskar, C. V. N., Pal, S., and Pattnaik, P. K., "Recent Advancements in Fiber Bragg Gratings Based Temperature and Strain Measurement," *Results in Optics*, Vol. 5, 2021, p. 100130. https://doi.org/10.1016/j.rio.2021.100130.

[32] Wang, H., Wu, X., Huang, Z., and Xing, E. P., "High-Frequency Component Helps Explain the Generalization of Convolutional Neural Networks," *2020 IEEE/CVF Conference on Computer Vision and Pattern Recognition (CVPR)*, IEEE, New York, USA, 2020, pp. 8681–8691. https://doi.org/10.1109/CVPR42600.2020.00871.